

# Multibioinspired Soft Grasping Actuators with Laser-Induced Multiscale Microstructures

Chenchu Zhang,\* Linhan Zhao, Renfei Chen, Rui Cao, Qiangqiang Zhao, Chaowei Wang, Ying Hu,\* and Dong Wu

Soft robotics has been widely adopted in numerous applications of soft grippers, which utilize compliance to achieve superior grasping performances with excellent simplicity, adaptability, and robustness. The critical concerns for soft grippers are insufficient grasping ability and the limitation of functions. Herein, a multibionic soft gripper with multiscale microstructures is demonstrated, featuring light weight (12 mg), versatility, and endurance to heavy dust. The multibionic gripper mimics the grasping structure of eagle claws, the friction-increasing structure of gecko feet, and the shining structural color on butterfly wings. External laser stimuli allow the grasping of various objects and precise measurement of the target sizes. The soft actuator realizes a systematic bionic function rather than a single bionic function, providing new possibilities for miniaturization, environmental adaptation, and multifunctionality of grasping actuators.


## 1. Introduction

Soft actuators have attracted extensive interest and intensive research due to their superiority in simulating biological behaviors.<sup>[1,2]</sup> Soft actuators made of soft materials are expected to perform tasks in unstructured environments due to their soft

C. Zhang, L. Zhao, R. Chen, Q. Zhao, Y. Hu  
Anhui Province Key Lab of Aerospace Structural Parts Forming Technology and Equipment, Institute of Industry and Equipment Technology  
Hefei University of Technology  
Hefei 230009, China  
E-mail: hfutzcc@hfut.edu.cn; huying@hfut.edu.cn

R. Cao  
Caltech Optical Imaging Laboratory  
Andrew and Peggy Cherng Department of Medical Engineering  
California Institute of Technology  
Pasadena, CA 91125, USA

C. Wang, D. Wu  
CAS Key Laboratory of Mechanical Behavior and Design of Materials  
Department of Precision Machinery and Precision Instrumentation  
University of Science and Technology of China  
Hefei 230027, China

 The ORCID identification number(s) for the author(s) of this article can be found under <https://doi.org/10.1002/aisy.202200103>.

© 2022 The Authors. Advanced Intelligent Systems published by Wiley-VCH GmbH. This is an open access article under the terms of the Creative Commons Attribution License, which permits use, distribution and reproduction in any medium, provided the original work is properly cited.

DOI: 10.1002/aisy.202200103

and deformable bodies.<sup>[3]</sup> Compared with rigid manipulators, soft manipulators are usually lighter and smaller with more degrees of freedom. Therefore, they can easily complete diverse grasping tasks and can be applied to grasp fragile items, which is challenging for rigid manipulators.<sup>[4–8]</sup> These characteristics make soft manipulators ideal choices in applications in a complex environment.

In recent years, biomimetic soft actuators have been widely studied due to their excellent flexibility and maneuverability, showing great potential and broad application prospects.<sup>[9–14]</sup> Soft actuators can be driven by various external stimuli, such as light,<sup>[15–17]</sup> temperature,<sup>[18]</sup> magnetic field,<sup>[19]</sup> humidity,<sup>[20]</sup> electricity,<sup>[21]</sup> pH,<sup>[22]</sup> or multiple stimuli,<sup>[23–25]</sup> to achieve differ-

ent functions, such as grasping,<sup>[26]</sup> crawling,<sup>[27]</sup> jumping,<sup>[28]</sup> swimming,<sup>[29]</sup> obstacle crossing,<sup>[30]</sup> and rolling.<sup>[31]</sup> Among the earlier functions, the grasping of soft actuators has drawn the attention of researchers due to the better flexibility and capability of grasping fragile objects harmlessly than conventional rigid grippers. Light has several advantages compared with other stimuli.<sup>[16,23,32,33]</sup> For example, it can realize long-distance and wireless control with the freely adjusted intensity. In addition, light can illuminate different parts of the actuator according to the needs of the task, thereby stimulating the actuator to respond accordingly. For example, Deng et al. proposed a light-driven flexible robotic arm based on an aligned carbon nanotube (CNT)/paraffin wax composite layer that can achieve the functions of extending/contracting and grasping/releasing objects.<sup>[32]</sup> Chen et al. proposed a grasping actuator with an integrated sensing function based on reduced graphene oxide, paper, and a biaxially oriented polypropylene composite that can monitor its states in action through the change of resistance.<sup>[33]</sup> Lan et al. proposed that a UV-driven soft actuator based on liquid crystalline networks can achieve continuous action of grasping, lifting, transferring, and releasing a stick-like object by curling and stretching.<sup>[34]</sup> In addition, Tao et al. proposed a gecko-like structure on polydimethylsiloxane (PDMS), which can be used to capture objects in a clean vacuum environment.<sup>[35]</sup> Dong et al. proposed a humidity-driven eagle claw-like actuator.<sup>[36]</sup> The actuator can maintain an open state at lower humidity and can bend inward to grasp objects when the humidity increases. However, most of the grasping actuators mentioned before only demonstrate grasp-and-release functionality, and

the grasping force provided was generally insufficient. Moreover, the environmental robustness and the dust resistance of existing grasping actuators are far from ideal, resulting in a sharp decrease in grasping force in undesired environments such as heavy dust. Thus, how to improve the functionality and dust resistance of soft grippers and further realize bionic actuators with multiple functions remains challenging.

Biological systems present various amazing examples of adaptive and active behaviors. Eagles can efficiently hunt with the delicate structure of their claws. Their claws can flexibly extend and close in four different directions to firmly grasp the prey. Geckos can easily crawl on eaves, walls, and many other surfaces.<sup>[37–39]</sup> This is attributed to the evenly distributed layered microstructures on the surface of their feet,<sup>[35]</sup> which allow geckos to obtain enough friction force during climbing. The wings of butterflies have intriguing mimetic patterns, consisting of countless microstructures. When illuminated by sunlight, these microstructures can display bright structural colors.<sup>[40–42]</sup>

Inspired by these biological functions, a multiscale and tribo-mimetic soft actuator (MTSA) with microstructures varying from submicrometer to millimeter has been designed and fabricated to mimic the functions of eagle claws, gecko feet, and butterfly wings (**Figure 1**). The main body of the MTSA is a claw-shaped actuator (in the range of millimeters) imitating the eagle claw, while the gecko-like friction-enhancing sheets (in the range of micrometers) and the butterfly-like structural color sheets (in the range of hundreds of nanometers) are integrated into it. The claw-shaped actuator can perform a series of actions, such as grasping, transporting, and releasing objects, under the irradiation of near-infrared (NIR) light. The friction-enhancing sheets were integrated on the ends of the actuator's fingers by self-assembly with the help of van der Waals force to provide enough friction force and enhance the grasping ability. The structural color sheets were integrated on the outer surface of the actuator with the help of glue to show different colors based on the sizes of the grasped objects. Therefore, the size of an object can be measured by analyzing the wavelength of its structural color. In this study, the influence of NIR light power on the

actions of MTSA is investigated. In addition, the relationship between femtosecond (Fs) laser-processing parameters and the friction forces of friction-enhancing sheets is quantitatively analyzed, and the relationship between the structural color and the observation angle is systematically studied to support further measurements of the sizes of objects. Furthermore, the grasping capabilities of the MTSA in both clean/heavy dust environments are investigated and compared. In the end, the whole process of the grasping, releasing, and size sensing of objects is shown as a proof-of-concept demonstration.

## 2. Results and Discussions

### 2.1. Fabrication of Claw-Shaped Actuator, Friction-Enhancing Sheets, and Structural Color Sheets

Claw-shaped actuators were obtained by cutting a CNT/PDMS bilayered film using an Fs laser direct writing system. The shape of the actuator was designed to be a symmetrical four-finger structure inspired by the eagle's claw, which can apply a uniform grasp force around the grasped object. In terms of size design, the mechanical strength of the actuator will be reduced if the sizes of its fingers are too narrow, resulting in weak grasping capability. In addition, the bending state of four fingers will be non-uniform if the width of fingers is too wide,<sup>[43]</sup> as shown in Figure S1, Supporting Information. After full consideration, the sizes of the actuator fingers were designed to be  $8 \times 2$  mm, which can prevent the actuator from bending along a symmetry axis while ensuring its mechanical strength. In the fabrication process, the CNT/PDMS bilayered film was flatly placed on a glass slide for further cutting. The laser power and scanning times were set to 280 mW and 5 times, respectively. After cutting, the film was peeled off and attached to a handle to form the claw-shaped actuator (**Figure 2a**). When the NIR light (808 nm) irradiated the middle part of the actuator, the four finger-like structures can flatten to imitate the eagle's opened claws. When the NIR light was turned off, they bent inward to imitate the eagle's closed claws, as shown in Figure 2b and

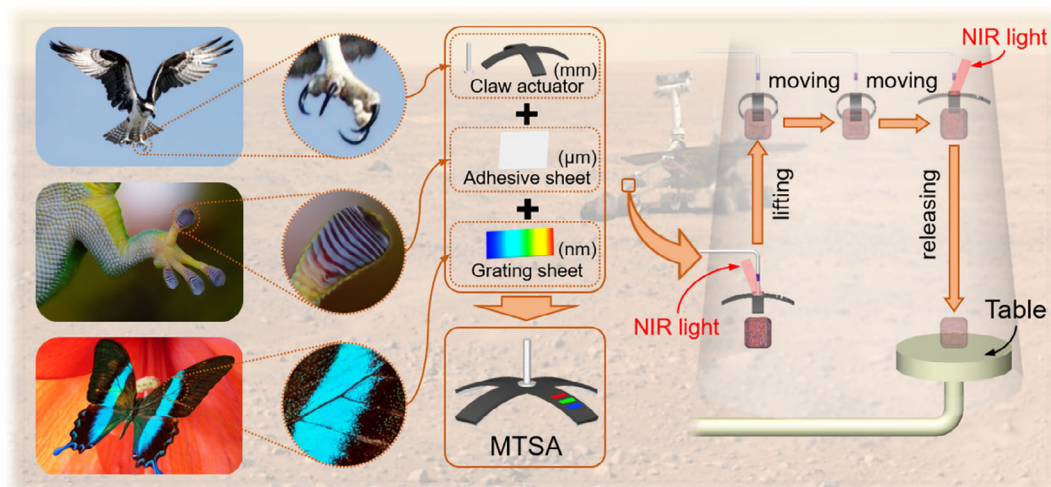


**Figure 1.** The design schematic diagram of MTSA and its application.

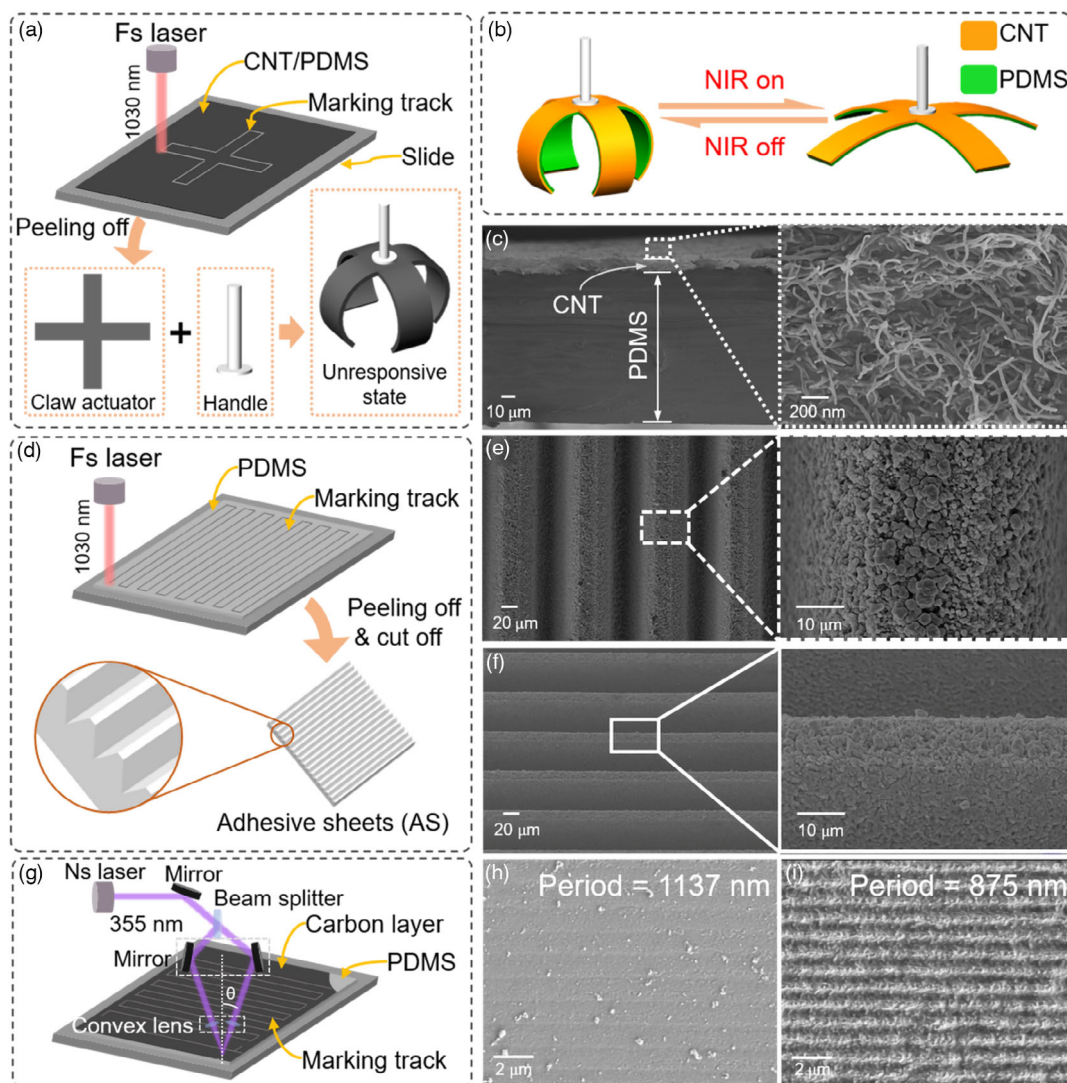


**Figure 2.** The fabrication and surface topography of the claw-shaped actuator, friction-enhancing sheets, and structural color sheets. a) The fabrication processing of the claw-shaped actuator in the fs laser direct writing system. b) The structural composition and schematic diagram of the claw-shaped actuator. c) SEM images of the claw-shaped actuator. d) The fabrication processing of the gecko-like friction-enhancing sheets in fs laser direct writing system. e, f) The SEM images of the top view and 45° tilted view of the gecko-like friction-enhancing sheets processed by fs laser. The scanning speed was  $8 \text{ mm s}^{-1}$ . g) The fabrication processing of structural color sheets in a nanosecond laser focusing interference processing system. h, i) SEM images of structural color sheets with different processing parameters,  $\theta_1 = 8.98^\circ$ ,  $W_1 = 0.25 \text{ mW cm}^{-2}$  in (h) and  $\theta_2 = 11.69^\circ$ ,  $W_2 = 0.45 \text{ mW cm}^{-2}$  in (i).

S2, Supporting Information. The claw-shaped actuator can respond quickly under irradiation with NIR light, mainly due to the excellent photothermal characteristics of the CNT/PDMS bilayer (Figure 2c). Under irradiation with NIR light, the stress generated by the CNT layer is greater than that generated by the PDMS layer, which will make the actuator bend toward the side of the CNT layer. When the NIR light is turned off, the bilayered film bends to the initial state.<sup>[31]</sup>

The friction-enhancing sheets were fabricated on PDMS films by an Fs laser direct writing system with a high-speed motion stage that can scan the X/Y coordinate directions. The laser power, scanning area, scanning space between two adjacent lines, and scanning times were set at 280 mW,  $5 \times 5 \text{ mm}$ ,

$100 \mu\text{m}$ , and 10 times to shape the microgroove structures. The scanning speeds were 2, 4, 6, 8, 10, and  $12 \text{ mm s}^{-1}$ , as shown in Figure 2d. The depth of the microgrooves can be controlled by simply changing the scanning speed of the Fs laser. Moreover, the microgrooves have a trapezoidal cross section with micronmeter-scale substructures distributed on top. The sizes of the microstructures decrease as the scan speed increases, while the number of microstructures decreases, as shown in Figure 2e, f, and S3, Supporting Information. These substructures, together with the microgrooves, determine the performance of the friction-enhancing sheets.

The structural color sheets were processed by the nanosecond laser interferometry processing system. First, the PDMS film was

cut to a suitable size and cleaned with absolute ethanol. Second, the carbon ink was drop cast on the surface of the PDMS film. Third, the carbon-coated PDMS film was placed in an oven for 30 min at 60 °C to form a carbon layer (Figure S4, Supporting Information). After that, the coated PDMS film was placed on the 2D moving stage to be processed by a focused interference light field. The moving speed of the 2D stage was 0.2 mm s<sup>-1</sup> (Figure 2g). The interference light field was formed by two converged coherent laser beams. Thus, the period of microgrooves can be modified by changing the interference angle  $\theta$  of the two laser beams. The fringe period  $D_s$  of the interference light field can be expressed as

$$D_s = \lambda / (2 \sin \theta) \quad (1)$$

Here, the wavelength of the ns laser was 355 nm. When the interference angle  $\theta$  increases, the fringe period  $D_s$  of the interference light field decreases. Two different sets of interference angles ( $\theta$ ) and power densities ( $W$ ) were selected:  $\theta_1 = 8.98^\circ$ ,  $W_1 = 0.25 \text{ mW cm}^{-2}$  and  $\theta_2 = 11.69^\circ$ ,  $W_2 = 0.45 \text{ mW cm}^{-2}$  based on our previous work.<sup>[44]</sup> The theoretical fringe periods of the corresponding interference light field were calculated to be 1137 and 875 nm, respectively. The scanning electron microscope (SEM) images of the structural color sheets processed by these two sets of processing parameters are shown in Figure 2h,i. Our measurement showed that the periods of the micro-/nanogrooves were  $1137 \pm 10 \text{ nm}$  and  $875 \pm 10 \text{ nm}$ , respectively, consistent with the theoretical values. However, due to the lower laser power density of the former sample group, the depth of the micro-/nanogrooves was too shallow to form bright colors. Thus, the latter fabrication parameters were chosen to process the structural color sheets. Considering that the structural color sheets may fail due to dust accumulation in heavy dust environments, the structural color sheets were covered by a layer of polyester (PET) film. With the help of PET's smooth surface and good thermal stability, it can prevent dust from accumulating on structural color sheets in a heavy dust environment with constant temperature changes. In addition, because PET has excellent optical properties, such as good light transmittance and low haze, it will not affect the application of structural color sheets, as shown in Figure S5, Supporting Information.

## 2.2. Properties of the Claw-Shaped Actuator

The claw-shaped actuators are essentially driven by the temperature-induced mismatched strains of the CNT films and PDMS films. Since it is difficult to reach a sufficiently high temperature ( $\approx 110^\circ\text{C}$ ) on the actuators by direct sunlight, the responses of the actuators are very weak under the irradiation of sunlight unless the light is focused by a convex lens, as shown in Figure S6, Supporting Information. In contrast, because of the high absorption and photothermal conversion of CNTs in the NIR spectrum, soft actuators can be precisely driven by a power-tunable NIR light. Therefore, NIR was chosen to stimulate the actuators. In the experiment, an NIR light irradiated the middle part of the claw-shaped actuator. Here, the distance (operating range) between the ends of two symmetrical fingers of the actuator was used to measure the response to the laser power. To better analyze the influence of the friction-enhancing

sheets on the light response of the actuator, claw-shaped actuators with and without friction-enhancing sheets have been prepared. In the initial state, the operating range of the former was 8.58 mm and that of the latter was 8.86 mm, which were extremely close. When the power of the NIR light increased from 0 to 300 mW with a gradient of 25 mW, the operating range of both actuators increased. When the NIR light power was 275 mW, the operating ranges of the two actuators were 17.15 and 16.67 mm, respectively, as shown in Figure 3a, Movie S1 and S2, Supporting Information. The results show that the friction-enhancing sheets have little effect on the light-response characteristics of the claw-shaped actuator. Figure S7, Supporting Information, shows the relationship of NIR power to temperature and operating range of the actuator. Clearly, a higher NIR power results in a higher temperature and larger operating range of the actuator. The maximum temperature was up to 106 °C, and the operating range was 17.15 mm when irradiated by NIR light (250 mW). Figure S8, Supporting Information, shows the real-time temperature changes of the actuator with irradiation of the NIR light (250 mW). The surface temperature of the actuator increased from 29 to 106 °C after 20 s of irradiation and returned to the initial temperature  $\approx 23 \text{ s}$  after turning off the NIR. The real-time IR images of the actuator actuation process with the irradiation of NIR (250 mW) are also presented in Figure S9, Supporting Information, which illustrate the reversible open-to-close actuation process and associated temperature changes. In addition, the actuators can still maintain a good response to NIR in a low-temperature ( $-18^\circ\text{C}$ ) environment, as shown in Figure S10, Supporting Information. In the study of the light-response property of the actuator, as shown in Figure 3b and Movie S3, Supporting Information, the operating range increased from the initial 8.76 to 16.52 mm when the actuator was irradiated by a 250 mW NIR light for 11 s and decreased to 9.35 mm after the NIR light was turned off for 16 s. It should be noted that within the first 5 s of NIR irradiation, the increment of the operating range of the actuator reached 90% of the total increment, and within the first 10 s after turning off, the reduction of the operating range of the actuator also reached 90% of the total reduction, which demonstrated the fast responsiveness of the actuator. In addition, the claw-shaped actuator integrated with friction-enhancing sheets was repeatedly irradiated by 250 mW NIR light for 100 cycles to show excellent stability (Figure 3c).

## 2.3. Properties of the Friction-Enhancing Sheets

To analyze the influence of fabrication parameters (fs laser scanning speed: 0, 2, 4, 6, 8, 10, and 12 mm s<sup>-1</sup>, other processing parameters unchanged) on the friction forces of friction-enhancing sheets, a homemade friction force measurement device was set. The device was mainly composed of a weight, fixed pulley, aluminum block, glass slides, upper splint, lower splint, and tensiometer to test the maximum static friction force shown in Figure S11, Supporting Information. The principle of the friction force measurement is shown in Section S1, Supporting Information.

Here, the properties of friction-enhancing sheets were tested in both clean/heavy dust environments. First, the friction-enhancing sheets were tested in a clean environment. The



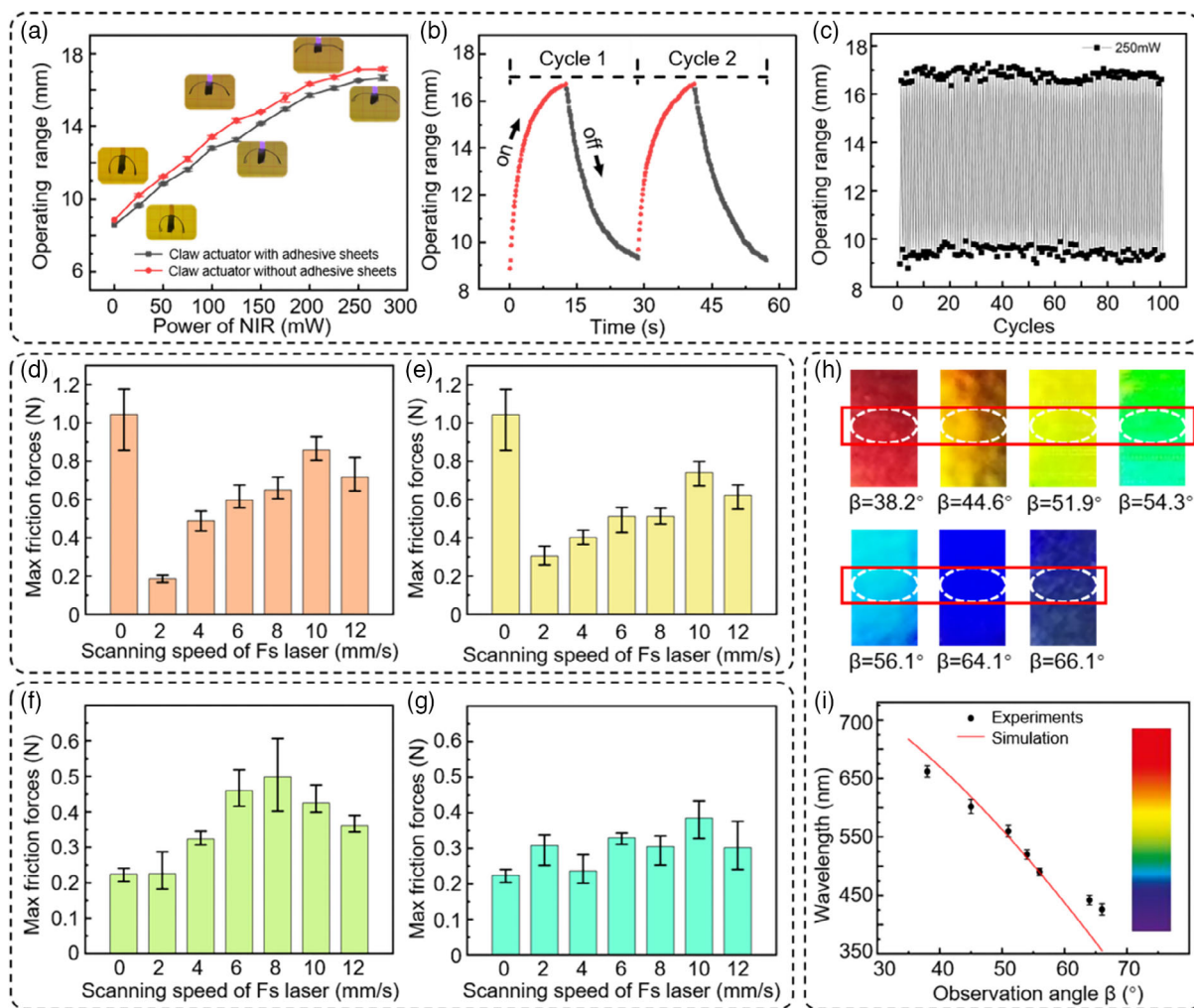


**Figure 3.** The properties of the claw-shaped actuator, friction-enhancing sheets, and structural color sheets. a) The photothermal response characteristics of MTSA. b) The cyclic operating range versus irradiation time curves of MTSA. c) The cycle versus operating range curves of the MTSA. d, e) The influence of the scanning speed of the fs laser on the friction forces of friction-enhancing sheets in a clean environment. The friction force tested in the direction perpendicular to the microgrooves is shown in (d). The friction force tested when the direction of the tension was parallel to the fabricated microgrooves is shown in (e). f, g) The influence of the scanning speed of the fs laser on the friction force of friction-enhancing sheets in a heavy dust environment. The friction force tested when the direction of the tension was perpendicular to the fabricated microgrooves is shown in (f). The friction force tested when the direction of the tension was parallel to the fabricated microgrooves is shown in (g). h) The structural colors at different observation angles  $\beta$ . i) The theoretical curves and experimental points of the relationship between the sample center structural color and observation angle  $\beta$  when the diffraction order  $n = 1$ .

maximum friction forces of friction-enhancing sheets (processed by different fs laser scanning speeds: 0, 2, 4, 6, 8, 10, and 12  $\text{mm s}^{-1}$ ) were tested along the direction perpendicular to the fabricated microgrooves. The maximum friction forces were 1.045, 0.186, 0.49, 0.597, 0.65, 0.859, and 0.717 N, respectively (Figure 3d). It is obvious that the 1.111 N friction force of the unprocessed (had not been processed by the Fs laser) friction-enhancing sheet was the largest. This was mainly due to the van der Waals force on the clean PDMS surface. The friction-enhancing sheet made at a scanning speed of 2  $\text{mm s}^{-1}$  produced the smallest friction force, which was only 0.196 N (Figure S12a, Supporting Information). With the increase of scanning speed, the maximum friction forces generally showed an increasing trend. In addition, the maximum friction forces of

the friction-enhancing sheets (processed by different Fs laser scanning speeds: 0, 2, 4, 6, 8, 10, and 12  $\text{mm s}^{-1}$ ) were tested along the direction parallel to the fabricated microgrooves and had similar properties. The maximum friction forces were 1.045, 0.304, 0.402, 0.511, 0.511, 0.741, and 0.622 N, respectively (Figure 3e). The friction force of the unprocessed friction-enhancing sheet was the largest. Meanwhile, the friction-enhancing sheet made at a scanning speed of 2  $\text{mm s}^{-1}$  produced the smallest friction force, which was only 0.33 N, as shown in Figure S12b, Supporting Information.

To investigate the performance degradation of the friction-enhancing sheet in heavy dust environments, the friction-enhancing sheets were tested after being treated with dry grass ash. The friction-enhancing sheets were processed

by different  $F_s$  laser scanning speeds at 0, 2, 4, 6, 8, 10, and 12 mm s<sup>-1</sup>. First, the maximum friction forces were tested along the direction perpendicular to the fabricated microgrooves, which were 0.224, 0.225, 0.323, 0.46, 0.498, 0.425, and 0.361 N, respectively, as shown in Figure 3f. Because the van der Waals force did not work in heavy dust environments, the friction force of the unprocessed friction-enhancing sheet decreased sharply compared with that of the clean sheet, which was only 0.256 N. The friction-enhancing sheet produced by the scanning speed of 8 mm s<sup>-1</sup> generated the largest friction force, which was 0.553 N, as shown in Figure S13a, Supporting Information. Moreover, the maximum friction forces increased as the scanning speed increased from 2 to 8 mm s<sup>-1</sup> but decreased gradually when the scanning speed was greater than 8 mm s<sup>-1</sup>. When the friction-enhancing sheets (processed by different  $f_s$  laser scanning speeds: 0, 2, 4, 6, 8, 10, and 12 mm s<sup>-1</sup>) were tested along the direction parallel to the fabricated microgrooves, the maximum friction forces were 0.224, 0.308, 0.236, 0.329, 0.305, 0.385, and 0.302 N, respectively, as shown in Figure 3g. Similar to the previous results, the friction force of the unprocessed friction-enhancing sheet was the smallest. Meanwhile, the friction-enhancing sheet made at a scanning speed of 10 mm s<sup>-1</sup> produced the largest friction force of 0.409 N, as shown in Figure S13b, Supporting Information.

From the earlier experimental results, it can be concluded that friction-enhancing sheets with layered microgrooves have obvious anisotropy in both clean/heavy dust environments. In general, the friction-enhancing sheets with microgrooves can produce superior friction force in the direction perpendicular to the microgrooves. In addition, although the unprocessed sheets have shown a good friction-enhancing ability in clean environments, the friction forces dropped sharply in heavy dust environments, while the processed ( $f_s$  laser scanning speed was 8 mm s<sup>-1</sup>) one maintained higher friction forces in both clean/heavy dust environments. For example, the former maximum friction force was dropped to 0.232 N in a heavy dust environment, which was only 20.8% of that in clean environments. In contrast, the maximum friction force of the latter was 0.553 N in heavy dust environments, which maintained 80.9% of the friction force in a clean environment and showed good stability. Moreover, the friction forces of the latter were 238% of the former in heavy dust environments.

## 2.4. Properties of the Structural Color Sheets

When a structural color sheet was irradiated by an LED lamp at a fixed angle, it could show different colors at different observation angles  $\beta$ , defined as the angle between the camera and the XY plane, as shown in Figure S14, Supporting Information. In this experiment, the structural color sheet with microgrooves was placed flatly on a horizontal table. An LED lamp was used to irradiate vertically above the structural color sheet. A camera was set on the right side of the structural color sheet to record the structural colors at different observation angles. To facilitate the quantitative characterization of the structural color sheets, we simplified the periodic microgroove structure as a rectangular reflection model. Then, the diffraction spectrum can be deduced from theoretical analysis, and the relationship between the

wavelength of structural colors and the observation angle  $\beta$  can be expressed as

$$n\lambda_w = T(\sin \alpha \pm \cos \beta) \quad (2)$$

Here, the diffraction order  $n = 1$ , the wavelength range of the observed light is 400 nm <  $\lambda_w$  < 700 nm, and the period of microgrooves  $T = 875$  nm. The incident angle ( $\alpha$ ) is 0 because the light was incident perpendicular to the structural color sheet. Only the observation angle  $\beta$  was changed in the experiment. When the observation angles were 38.2°, 44.6°, 51.9°, 54.3°, 56.1°, 64.1°, and 66.1°, the structural colors were red, orange, yellow, green, indigo, blue, and purple, respectively (Figure 3h). The wavelengths of all structural colors were measured by a spectrometer to be 662, 602, 572, 528, 488, 442, and 426 nm, consistent with the wavelengths calculated by the above formula (Figure 3i). The errors may be caused by deviations in the incident angle.

## 2.5. Analysis of the Weights and Sizes of Objects Grasped by MTSA

To test the grasping and sensing ability of the actuator, a multiscale biomimetic soft actuator (MBSA) composed of a claw-shaped actuator and structural color sheets (Figure 4a) and an MTSA composed of a claw-shaped actuator, structural color sheets, and friction-enhancing sheets (Figure 4b) were analyzed and compared. The experimental results showed that the MBSA could grasp cubes with a size of 7–10 mm, as shown in Figure S15, Supporting Information. When the sizes of the objects were less than 7 mm, which was close to the minimum opening size of the MBSA, the gripper could not produce enough friction force to the object and tended to release it. When the sizes of the object were larger than 10 mm, it was close to the maximum opening range of the MBSA, making the contact area too small to provide enough friction force. In addition, when the sizes of objects were 7, 8, 9, and 10 mm, the maximum weights that could be grasped by MBSA were 20, 23, 71, and 47 mg, respectively, as shown in Figure S15, Supporting Information. However, the MBSA can only grasp objects within a relatively narrow size range (8–9 mm) after being treated with grass ash. The corresponding maximum grasping weights of them were also reduced greatly, which were 13 and 21 mg, respectively, as shown in Figure S16, Supporting Information. This was mainly due to the sharply decreased van der Waals force of MBSA in a heavy dust environment. Meanwhile, to test the grasping ability of the MTSA, an MTSA1 with friction-enhancing sheets that had not been processed by  $f_s$  laser and an MTSA2 with friction-enhancing sheets processed by  $f_s$  laser (scanning speed was 8 mm s<sup>-1</sup>) were chosen. It showed that both MTSA1 and MTSA2 could grasp objects within the size range between 4 to 10 mm in a clean environment. When the sizes of the objects were 4, 5, 6, 7, 8, 9, and 10 mm, the maximum grasping weights of MTSA1 were 13, 46, 97, 120, 153, 171, and 47 mg, respectively. Meanwhile, the maximum grasping weights of MTSA2 were 13, 56, 57, 110, 173, 141, and 47 mg, respectively (Figure 4c). The results showed that the laser-processed microgrooves had little influence on the grasping capability of the MTSA in clean environments. However, after

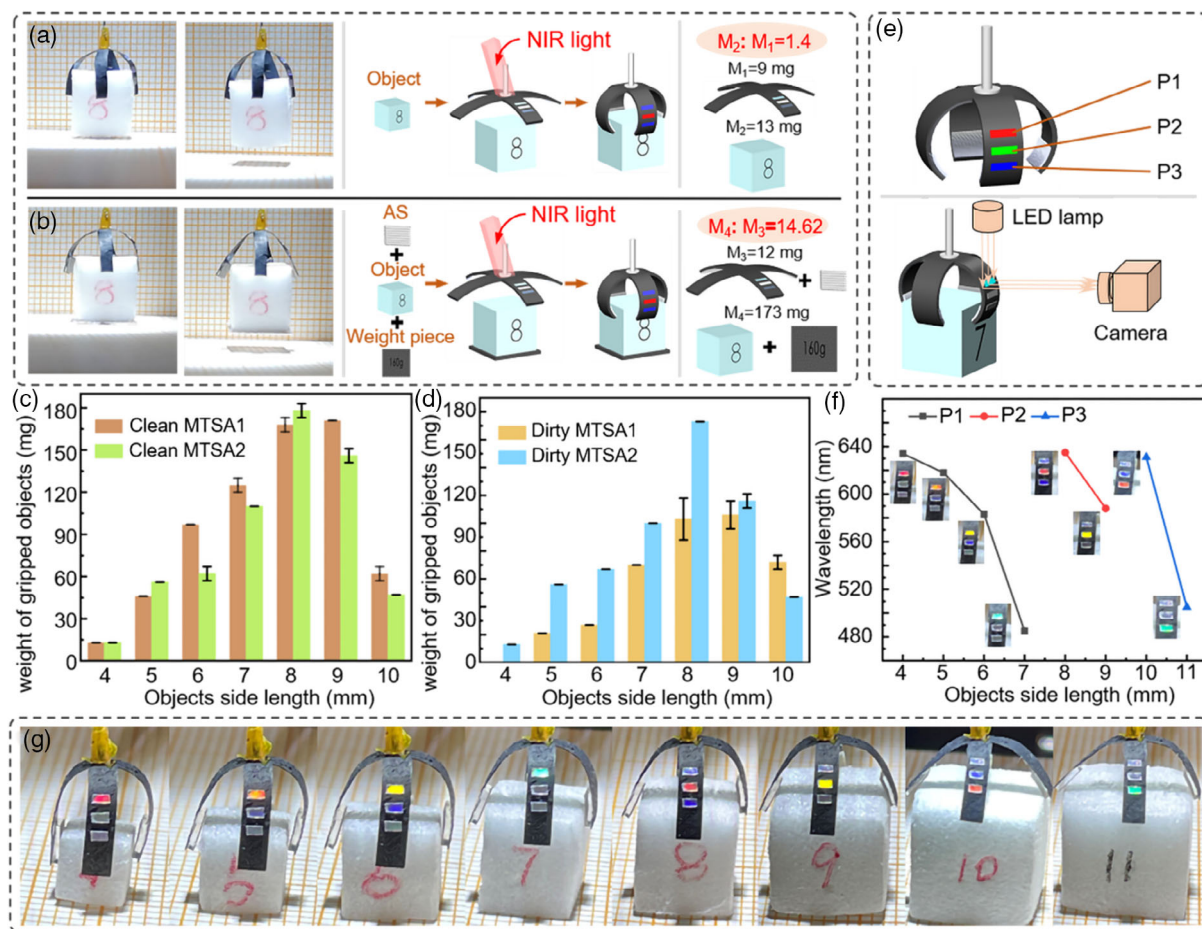


**Figure 4.** Analysis of the weights and sizes of objects grasped by the MTSA. a,b) The maximum weight of objects (the size was 8 mm) can be grasped by MBSA (a) and MTSA2 (b) in a heavy dust environment. The maximum weights of objects with different sizes (4, 5, 6, 7, 8, 9, and 10 mm) can be determined by MTSA1 and MTSA2 in a clean environment (c) and heavy dust environment (d). e) The schematic diagram of measuring the sizes of objects by the structural colors and the areas of structural color sheets. f,g) The correspondence among the color areas, the wavelengths of the structural colors, and the sizes of the objects.

being treated with grass ash, the grasping capability of MTSA1 and MTSA2 was noticeably different. First, MTSA1 can grasp objects with a size of 5–10 mm. Meanwhile, the grasped size range of MTSA2 was 4–10 mm. Second, when the sizes of the objects were 4, 5, 6, 7, 8, 9, and 10 mm, the maximum grasping weights of MTSA1 were 0, 16, 27, 70, 83, 91, and 57 mg, respectively. The maximum grasping weights of MTSA2 were 13, 56, 67, 100, 173, 111, and 47 mg, respectively, as shown in Figure 4d. It can be concluded that MTSA2 has a significantly better grasping capability than MTSA1 in terms of antifouling ability. MTSA2 showed better performance in the captured size range and the maximum grasping weights in both clean/heavy dust environments. Remarkably, when the size of the grasped object was 8 mm, the maximum grasped weight of MTSA2 (12 mg) was 173 mg under heavy dust, which was 1462% of MTSA2's own weight (Figure 4b). However, under the same conditions, the maximum grasping weight of MBSA (9 mg) was 13 mg, which was only 140% of its own weight, as shown in Figure 4a. It can be concluded that integrating the friction-enhancing sheets processed by the fs laser on the claw-shaped actuator can significantly improve its grasping ability.

In the study of the correspondence between structural colors and object size, three structural color sheets (P1, P2, and P3) processed by the same processing parameters were evenly attached to the upper surface of the MTSA finger structure (Figure 4e). An LED lamp was placed vertically on the top of the MTSA with a camera set on its right side to record the corresponding color-rendering area and structural colors. According to the experimental results, when the sizes of the objects were 4, 5, 6, and 7 mm, only the P1 area had obvious structural colors, which were red, orange, yellow, and indigo with corresponding wavelengths of 634, 618, 583, and 485 nm, respectively. When the sizes were 8 and 9 mm, only the P2 area had obvious structural colors, which were red and yellow with corresponding wavelengths of 635 and 588 nm, respectively. When the sizes were 10 and 11 mm, only the P3 area had obvious structural colors, which were red and indigo with the corresponding wavelengths of 631 and 505 nm, respectively, as shown in Figure 4f,g. By establishing a corresponding relationship between the structural color area, the wavelength of the structural color, and the size of the object, the size of an object can be reliably determined by identifying the wavelength of the structural color.



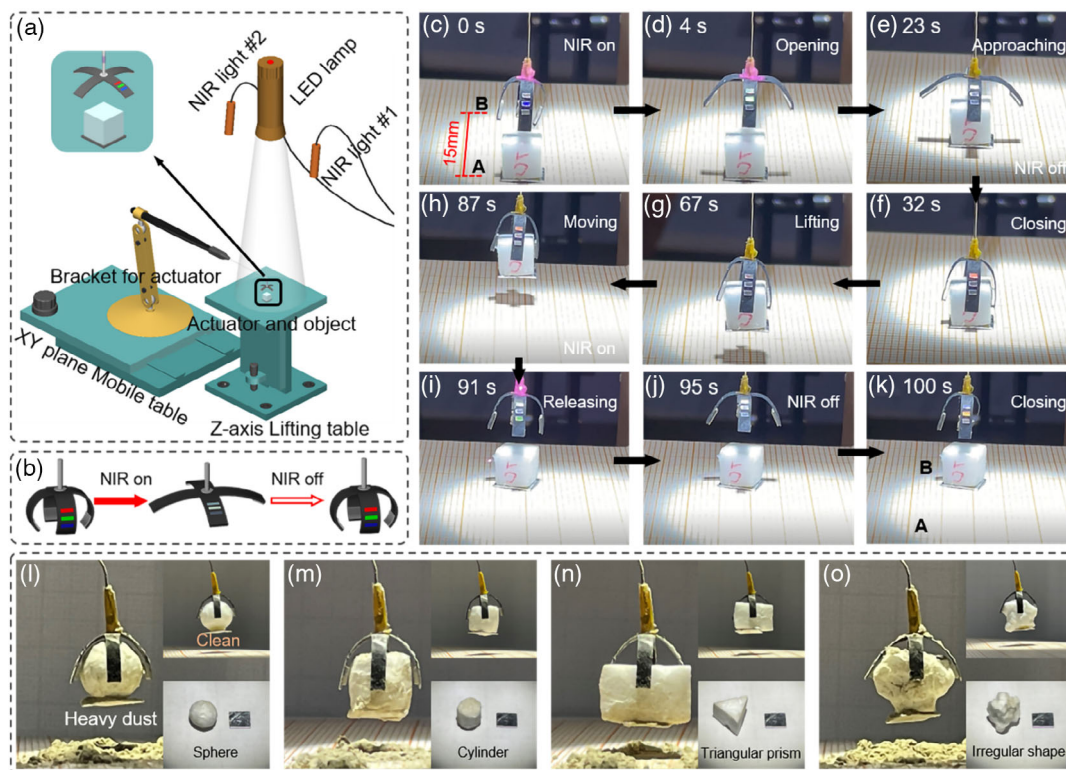


**Figure 5.** The whole process of object grasping, transferring, releasing, and size measurement. a) The homemade experimental device for testing the process of object grasping, transferring, releasing, and size measurement. b) The responses of MTSA with/without irradiation with the NIR light. c–k) The process of object grasping, transferring, releasing, and size measurement. l–o) Excellent performance in grasping spheres, cylinders, triangular prisms, and irregularly shaped objects in clean/heavy dust environments.

As a proof of concept, a homemade experimental device (Figure 5a) was set up to show the whole process of object grasping, transferring, releasing, and size measurement. The tested object was a cube with a size of 5 mm and a weight of 26 mg. The MTSA can open under irradiation with the NIR light and close inward after the NIR light was turned off, as shown in Figure 5b. The MTSA tried to move the object from place A to place B, which was 15 mm from place A, as shown in Figure 5c. Irradiated by NIR light #1 for 4 s, the MTSA opened to the graspable range and approached the object by raising the lift. Then, NIR light #1 was turned off and the MTSA firmly grasped the object in 9 s. Meanwhile, a camera recorded the structural color (P1, orange, and 620 nm) at this moment. After that, MTSA moved together with the object to transfer it to place B in  $\approx 20$  s. After the movement, NIR light #2 irradiated the MTSA to release the object. In the end, NIR light #2 was turned off when the object was released, as shown in Figure 5c–k and Movie S4, Supporting Information. The corresponding displays in the heavy dust environment are shown in Figure S17, Supporting Information. In addition, MTSA also has excellent performance in grasping objects of different shapes, such as spheres, cylinders, triangular prisms, and irregularly shaped objects, in both clean/heavy dust environments (Figure 5l–o), showing that the MTSA has wide applicability.

### 3. Conclusion

In summary, an MTSA composed of three kinds of biomimetic structures was fabricated. A CNT/PDMS-based claw-shaped actuator with excellent photothermal response characteristics was applied to imitate the behavior of the eagle claw to grasp objects. In addition, friction-enhancing sheets with microgrooves were applied to improve the grasping capability of MTSA in both clean/heavy dust environments. Moreover, butterfly-like structural color sheets were used for the measurement of object size. The proposal of MTSA helps to promote bionics from the single-structure bionic to the systematic bionic. Due to its light weight, small size, versatility, and adaptability to complex environments, it provides a solution to the problems of light weight, miniaturization, and functionalization of manipulators in aerospace and engineering. In addition, there are also potential applications in grasping objects, collecting samples, and measuring the size of objects in future space exploration.

### 4. Experimental Section

The detailed experimental section can be found in Section S2, Supporting Information.



## Supporting Information

Supporting Information is available from the Wiley Online Library or from the author.

## Acknowledgements

This work was supported by the National Natural Science Foundation of China (grant numbers 62105090 and 62005262); the China Postdoctoral Science Foundation (grant numbers 2020M671888 and 2021T140649); and Anhui Provincial Natural Science Foundation (grant number 2008085J22).

## Conflict of Interest

The authors declare no conflict of interest.

## Data Availability Statement

The data that support the findings of this study are available from the corresponding author upon reasonable request.

## Keywords

bionic microstructures, environmental adaptability, laser-induced multiscale microstructures, soft actuators

Received: April 27, 2022

Revised: July 17, 2022

Published online:

- [1] M. Z. Miskin, A. J. Cortese, K. Dorsey, E. P. Esposito, M. F. Reynolds, Q. K. Liu, M. C. Cao, D. A. Muller, P. L. McEuen, I. Cohen, *Nature* **2020**, *584*, 557.
- [2] C. Y. Xu, Z. L. Yang, S. W. K. Tan, J. H. Li, G. Z. Lum, *Adv. Intell. Syst.* **2022**, *4*, 2100259.
- [3] S. G. Nurzaman, F. Iida, L. Margheri, C. Laschi, *Soft Rob.* **2014**, *1*, 154.
- [4] D. Rus, M. T. Tolley, *Nature* **2015**, *521*, 467.
- [5] J. Shintake, V. Caccuciolo, D. Floreano, H. Shea, *Adv. Mater.* **2018**, *30*, 1707035.
- [6] M. G. Catalano, G. Grioli, E. Farnioli, A. Serio, C. Piazza, A. Bicchi, *Int. J. Rob. Res.* **2014**, *33*, 768.
- [7] Y. Bahramzadeh, M. Shahinpoor, *Sci. Rob.* **2014**, *1*, 38.
- [8] R. Deimel, O. Brock, *Int. J. Rob. Res.* **2016**, *35*, 161.
- [9] S. A. Morin, R. F. Shepherd, S. W. Kwok, A. A. Stokes, A. Nemiroski, G. M. Whitesides, *Science* **2012**, *337*, 828.
- [10] Y. Hu, Q. X. Ji, M. J. Huang, L. F. Chang, C. C. Zhang, G. Wu, B. Zi, N. Z. Bao, W. Chen, Y. C. Wu, *Angew. Chem. Int. Ed.* **2021**, *60*, 20511.
- [11] Y. Y. Song, Y. Liu, H. B. Jiang, J. Z. Xue, Z. P. Yu, S. Y. Li, Z. W. Han, L. Q. Ren, *ACS Appl. Mater. Interfaces* **2019**, *11*, 13742.
- [12] P. Glick, S. A. Suresh, D. Ruffatto, M. Cutkosky, M. T. Tolley, A. Parness, *IEEE Rob. Autom. Lett.* **2018**, *3*, 903.
- [13] J. R. Amend, E. Brown, N. Rodenberg, H. M. Jaeger, H. Lipson, *IEEE Trans. Rob.* **2012**, *28*, 341.
- [14] L. Y. Sun, Z. Y. Chen, F. K. Bian, Y. J. Zhao, *Adv. Funct. Mater.* **2020**, *30*, 1907820.
- [15] J. T. Miao, N. Y. Ge, Y. D. Wu, S. Q. Peng, L. H. Zheng, T. Y. Chou, L. X. Wu, *Chem. Eng. J.* **2022**, *427*, 131580.
- [16] L. Z. Chen, M. C. Weng, P. D. Zhou, L. L. Zhang, Z. G. Huang, W. Zhang, *Nanoscale* **2017**, *9*, 9825.
- [17] Y. Y. Yang, Y. T. Liu, Y. J. Shen, *Adv. Funct. Mater.* **2020**, *30*, 1910172.
- [18] S. X. Wei, W. Lu, X. X. Le, C. X. Ma, H. Lin, B. Y. Wu, J. W. Zhang, P. Theato, T. Chen, *Angew. Chem. Int. Ed.* **2019**, *58*, 16543.
- [19] W. Q. Hu, G. Z. Lum, M. Mastrangeli, M. Sitti, *Nature* **2018**, *554*, 81.
- [20] Q. Zhao, J. W. C. Dunlop, X. L. Qiu, F. H. Huang, Z. B. Zhang, J. Heyda, J. Dzubiella, M. Antonietti, J. Y. Yuan, *Nat. Commun.* **2014**, *5*, 4293.
- [21] Z. H. Zeng, H. Jin, L. P. Zhang, H. Zhang, Z. Chen, F. Gao, Z. Zhang, *Carbon* **2015**, *84*, 327.
- [22] C. X. Yang, F. Su, Y. Liang, W. Y. Xu, S. Li, E. X. Liang, G. X. Wang, N. B. Zhou, Q. Wan, X. G. Ma, *Soft Matter* **2020**, *16*, 2928.
- [23] M. C. Weng, P. D. Zhou, L. Z. Chen, L. L. Zhang, W. Zhang, Z. G. Huang, C. H. Liu, S. S. Fan, *Adv. Funct. Mater.* **2016**, *26*, 7244.
- [24] X. K. Li, J. Z. Liu, D. D. Li, S. Q. Huang, K. Huang, X. X. Zhang, *Adv. Sci.* **2021**, *8*, 2101295.
- [25] R. H. Yang, M. Jin, M. M. Jin, H. S. Qian, Q. Gao, G. Q. Jin, S. W. Zhang, *Adv. Intell. Syst.* **2021**, *3*, 2000146.
- [26] J. C. Breger, C. Yoon, R. Xiao, H. R. Kwag, M. O. Wang, J. P. Fisher, T. D. Nguyen, D. H. Gracias, *ACS Appl. Mater. Interfaces* **2015**, *7*, 3398.
- [27] H. J. Lu, M. Zhang, Y. Y. Yang, Q. Huang, T. Fukuda, Z. K. Wang, T. J. Shen, *Nat. Commun.* **2018**, *9*, 3944.
- [28] H. Arazoe, D. Miyajima, K. Akaike, F. Araoka, E. Sato, T. Hikima, M. Kawamoto, T. Aida, *Nat. Mater.* **2019**, *15*, 1084.
- [29] T. F. Li, G. R. Li, Y. M. Liang, T. Y. Cheng, J. Dai, X. X. Yang, B. Y. Liu, Z. D. Zeng, Z. L. Huang, Y. W. Luo, T. Xie, W. Yang, *Sci. Adv.* **2017**, *3*, e1602045.
- [30] X. M. Du, H. Q. Cui, T. T. Xu, C. Y. Huang, Y. L. Wang, Q. L. Zhao, Y. S. Xu, X. Y. Wu, *Adv. Funct. Mater.* **2020**, *30*, 1909202.
- [31] Y. Hu, G. Wu, T. Lan, J. J. Zhao, Y. Liu, W. Chen, *Adv. Mater.* **2015**, *27*, 7867.
- [32] J. Deng, J. F. Li, P. N. Chen, X. Fang, X. M. Sun, Y. S. Jiang, W. Weng, B. J. Wang, H. S. Peng, *J. Am. Chem. Soc.* **2016**, *138*, 225.
- [33] L. Z. Chen, M. C. Weng, P. D. Zhou, F. Huang, C. H. Liu, S. S. Fan, W. Zhang, *Adv. Funct. Mater.* **2019**, *29*, 1806057.
- [34] R. C. Lan, J. Sun, C. Shen, R. Huang, Z. P. Zhang, C. Ma, J. Y. Bao, L. Y. Zhang, D. K. Yang, H. Yang, *Adv. Funct. Mater.* **2020**, *30*, 2000252.
- [35] D. S. Tao, X. Gao, H. Y. Lu, Z. Y. Liu, Y. Li, H. Tong, N. Pesika, Y. G. Meng, Y. Tian, *Adv. Funct. Mater.* **2017**, *27*, 1606576.
- [36] Y. Dong, J. Wang, X. K. Guo, S. S. Yang, M. O. Ozen, P. Chen, X. Liu, W. Wei, F. Xiao, U. Demirci, B. F. Liu, *Nat. Commun.* **2019**, *10*, 4087.
- [37] K. Autumn, S. T. Hsieh, D. M. Dudek, J. Chen, C. Chitaphan, R. J. Full, *J. Exp. Biol.* **2006**, *209*, 260.
- [38] K. Autumn, M. Sitti, Y. A. Liang, A. M. Peattie, W. R. Hansen, S. Sponberg, T. W. Kenny, R. Fearing, J. N. Israelachvili, R. J. Full, *Proc. Natl. Acad. Sci.* **2002**, *99*, 12252.
- [39] K. Autumn, J. Puthoff, *Biological Adhesives*, Springer International Publishing, Switzerland **2016**.
- [40] P. Vukusic, J. R. Sambles, *Nature* **2003**, *424*, 852.
- [41] M. A. Giraldo, S. Yoshioka, C. Liu, D. G. Stavenga, *J. Exp. Biol.* **2016**, *219*, 3936.
- [42] H. Butt, A. K. Yetisen, D. Mistry, S. A. Khan, M. U. Hassan, S. H. Yun, *Adv. Opt. Mater.* **2016**, *4*, 497.
- [43] A. M. Abdullah, X. L. Li, P. V. Braun, J. A. Rogers, K. J. Hsia, *Adv. Mater.* **2018**, *30*, 1801669.
- [44] C. C. Zhang, R. F. Chen, L. L. Yang, H. Wu, S. Y. Ji, J. M. Zhang, L. H. Zhou, H. C. Ye, S. Z. Wu, J. J. Zhang, C. W. Wang, Y. Hu, *ACS Appl. Mater. Interfaces* **2020**, *12*, 45641.